#25-102
2025 AFS Proceedings ©American Foundry Society

Effect of Section Size and Cooling Rate Variation in the Microstructure of Al-Ce-Ni-Graphite Composites

Kaustubh Kishore Rane, Swaroop Kumar Behera,
Mehran Zare, Alec Thaddeus Buhler, Luke Malone Wilson
Department of Materials Science & Engineering, University of Wisconsin–Milwaukee, Milwaukee, Wisconsin, USA

David Weiss
Vision Materials, Manitowoc, Wisconsin, USA

Benjamin Church, Pradeep Rohatgi
Department of Materials Science & Engineering, University of Wisconsin–Milwaukee, Milwaukee, Wisconsin, USA

ABSTRACT

The effect of cooling rate variation on the microstructure and properties of Al-12Ce-2.5Mg alloy reinforced with Ni-graphite has been presented in this study. The composite melt prepared by stir mixing was cast in a preheated permanent step mold wherein the section size varied from 3.7 mm to 30 mm. The distribution of graphite, primary and eutectic phases, hardness, and density have been studied as a function of section size and cooling rate. The volume percentages of intermetallic phases changed with an increase in section size, and the hardness decreased with an increase in section size, suggesting that other mechanical properties are a function of section size and cooling rate. The results were compared with those of the Al-12Ce-2.5Mg base alloy cast using the same process to understand the effects of Ni-graphite additions on the microstructure and properties of Al-12Ce-2.5Mg alloy in different sizes.

Keywords: aluminum-cerium, stir-casting, composites, cooling rate, Ni-graphite

INTRODUCTION

ALUMINUM ALLOYS

Aluminum is a desirable material in structural design. It boasts many great mechanical properties such as high strength, low weight and density, high ductility, environmental survivability granted by high corrosion and wear resistance, thermal properties including low coefficient of thermal expansion (CTE) and excellent thermal conductivity, and feasibility of use such as low cost, good availability, outstanding castability, and a desirable melting temperature that allows for many applications while not impairing desirable fabrication processes. Aluminum alloy components are highly valued where weight reduction is key, as in automotive and aerospace design.[1–8] It is in part because aluminum has so many desirable properties that it is also a sought-after base metal for alloying with other elements to alter or add certain properties while retaining many of its original properties, whether mechanical, chemical, or electrical, to fit a specific purpose. Properties of aluminum alloys include good weldability, low cost, extreme recyclability, excellent physical and mechanical properties (low density, high thermal conductivity, high strength-to-weight ratio), ease of processing, good corrosion resistance, and excellent castability.[9–11] When it comes to manipulating the alloy, there are two main methods; the elemental composition of the alloy can be changed in order to introduce new phases to the material, creating hypoeutectic, eutectic, or hypereutectic materials; the second, more impactful method is controlling the cooling rate of the material, which both controls the microstructure and morphology of a material as well as its thermal conductivity, all of which have a large deciding factor on the physical and mechanical properties of a material.

Aluminum alloys are used in automotive and aerospace industries, but because of altered traits due to alloying, their scope of use can be expanded, for example, 6xxx-series (Al-Mg-Si) are also used in marine and construction industries due to higher corrosion resistance, formability, and lower cost compared to other aluminum alloys; and high-strength aluminum alloys are also used in critical components in marine and even cryogenic industries.[11,12] Common elements alloyed with aluminum can be broken into major (Si, Cu, Mg, Zn) and trace (Mn, Ti, Cr, V, Sc etc.) alloying elements.[10] However, while aluminum alloys do have many desirable mechanical properties, when they are brought to higher temperatures, around 752F (400C), those properties suffer significantly. This can be a problem when using aluminum alloys in particular areas, such as automotive and aerospace, where high temperatures are desired to increase fuel efficiency.

ALUMINUM – CERIUM SYSTEM

Thermal stability defines a material's resistance to permanent property changes caused solely by heat.[13]

Different elements have been used in aluminum alloys to remedy the issue of loss of mechanical properties at higher temperatures, these include Ti, Zr, V, Mo, Mn, and Cr.[14] The main indicator that an element will provide good thermal stability to the base element is its diffusivity with it.[15] Silicon and nickel are commonly alloyed with aluminum, but cerium has become a popular alternative partly because it has a diffusion coefficient that is 6 and 4 orders of magnitude lower compared to silicon and nickel, respectively.[14] Cerium, as a major alloying element of aluminum, results in an alloy with a lower liquidus temperature, improved thermal stability, and high-temperature resistance to creep.[8] Furthermore, cerium additions to aluminum and aluminum alloys have proved to increase other properties at room and elevated temperatures, both chemical and mechanical, as well as increasing castability: strength and elongation are improved with the addition of Ce, although the source of these improvements differs with minor and greater Ce contents; there is also marked improvement in wear and corrosion resistance given by Ce additions; the exothermic formation of Al-Ce phases leads to increased melt fluidity.[16,17] Cerium additions to aluminum alloys allow for lots of versatility, as the increase in thermal stability is independent of the production method, as well as Ce reacting favorably with many other elements, leading to a wide array of usable ternary and quaternary Al-Ce alloys.[8,18]

ALUMINUM BASED METAL MATRIX COMPOSITES (AMC)

Prior literature has discussed multiple methods for the fabrication of aluminum matrix and particle-reinforced composites, as shown in Table 1 (in the Appendix). Based on the nature of the particles, the prepared composite can be tailored to the application, such as the addition of graphite particles for improving the tribological properties, increased hardness, thermal properties, etc. Factors such as the volume fraction of the reinforcement of the composite are based on the fabrication method. In the case of pressure infiltration or hot press sintering, a higher volume fraction of reinforcement is observed, while stir-casting can incorporate a lower volume fraction of the reinforcement. On account of poor wettability between aluminum and graphite, a rejection of the reinforcement particles is observed, resulting in the failure of reinforcement incorporation in the metal matrix. In order to mitigate this issue, the graphite particles are coated with nickel or copper, increasing the wettability of the graphite reinforcements. In the case of pressure infiltration or stir-casting, the presence of a suitable wettability-enhancing agent, such as a coating of copper or nickel on the surface of the reinforcement or the addition of Mg as an alloying element to the melt, will further the bond between the matrix and reinforcement and provide better properties. This is especially true in the case of ceramic reinforcements such as SiC or Al_2O_3, which have been discussed in previous studies.[19,20] The presence of select reinforcements, such as graphite or hollow spheres of Al_2O_3, can also help in reducing the density of the composite compared to the base alloy. Syntactic foams with hollow Al_2O_3 spheres have previously infiltrated via the pressureless route.[21,22] Such foams can find applications for the absorption of shock waves, as the presence of hollow particles would lead to the breakdown of propagating waves. Metal matrix composites can find further applications by utilizing byproducts from other industries, such as fly ash from power plants and used sand from foundries, as reinforcement agents, thus extending their applications and providing a cost-effective outlet for multiple industries.[23–27]

MATERIALS AND METHODS

MATERIALS

The step mold castings were made at Eck Industries using Al-12Ce-2.5Mg as the base alloy. The reinforcement was added in the form of nickel-coated graphite (60 wt.% Ni and 40 wt.% graphite) totaling 4 wt.%. The 500 lb. (226.796 kg) melt was stirred at 1382F (750C) during the reinforcement addition to ensure uniform distribution and prevent agglomeration. Nitrogen gas, at 0.35 MPa, was used for the degassing process with a degassing rod diffuser. The melt was poured into a permanent die mold that was preheated to 716F (380C) to form castings shown in Figure 1 and the cooling rates are shown in Table 2.

Table 2. Cooling Rates for Casting Sections

Section	Section Thickness (inches)	Cooling Rate (K/s)
A	0.14	67.5
B	0.28	22
C	0.57	11
D	1.15	3.7

A step mold provides a way to study the solidification of the melt at varying cooling rates in the presence of reinforcement particles. This variation in cooling rate is on account of the varying thickness of the cross sections. In this work, the smallest section size was 0.14 in. in thickness, while the largest section size was 1.15 in. in thickness as shown in Figure 1.

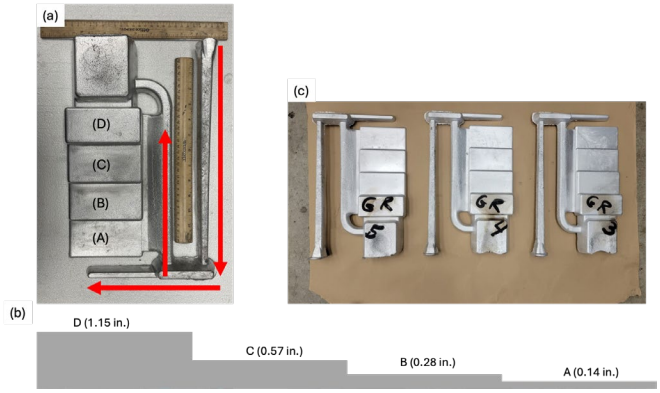

Figure 1. (a) Al-12Ce-Ni-Graphite composite step mold cast using the stir-casting technique. Sections A - D indicate the sections with varying thicknesses, (b) Schematic of the step mold showing the varying section thicknesses.

The sample was studied in as-cast condition, and each section of the casting was utilized for the measurement of density, volume percentage of phases, and hardness in order to understand the effect of varying cooling rates on the mechanical properties and microstructural evolution of the composite.

METHODS

The samples were metallographically prepared and were analyzed in unetched and etched conditions. The etchant utilized for the samples was Keller's reagent, with an etching time of 10 seconds. Optical microscopy was used to study the phase formation, and image analysis was done to measure the volume percentages of primary aluminum, graphite, intermetallic particles, eutectic phase, and porosity. The image analysis was performed using Clemex Vision and ImageJ using grey thresholding. The hardness of the composite was measured using Rockwell hardness F scale (HRF) measurements and was compared to cast Al-12Ce base alloy and pure aluminum. HRF was used due to constraints in the data, which originally measured in Rockwell hardness B scale (HRB) lay outside the recommended 20-100 (any scale), returning values sub twenty, and as HRF returns higher values overall, it was favored in this instance. Scanning electron microscopy (SEM) and energy dispersive spectroscopy (EDS) were conducted using a JEOL 6460LV with an acceleration voltage of 15 eV and were used for the quantification of the composite composition and to analyze the dissolution of nickel into the base alloy. Bruker D8 Discover X-ray Diffractometer was used for X-ray diffraction (XRD) to identify the phases, including $Al_{11}Ce_3$ and Al_3Ni, formed during the solidification process. The system was set up for 40 V and 40 Amp with a Cu element having a kα1 wavelength of 1.504 Å and a Ni filter for kα2 radiation. The density measurements were done with a Mettler Toledo AT261 using a density kit.

RESULTS AND DISCUSSIONS

MICROSTRUCTURAL ANALYSIS

As the section size of the step mold increases, thus decreasing the cooling rate, the area percentages of phases formed in the composite change with section size. In section A, as observed in Figure 2 (in the Appendix), with the fastest cooling rate, there is a higher area percentage of the eutectic phase as compared to section D. The area percentage of α-Al increases with an increase in section size with the slowest cooling rate having the largest area percentage. Two distinct intermetallic particles were identified in the sections, $Al_{11}Ce_3$ and Al_3Ni, the latter formed on account of the Ni addition to the matrix due to the dissolution of Ni from Ni-Graphite powder. In prior literature, the eutectic point of the Al-Ce system has been reported at varying concentrations of Ce, including 10.61 wt.% Ce, 12.2 wt.% Ce, 17.8 wt.% Ce, and 12 wt.% Ce.[28–30] Even at the fastest cooling rates, large primary intermetallic were observed to form, with a preference for nucleating close to the graphite particles. This nucleating phenomenon was observed in the remaining sections, wherein the reinforcement particles acted as a nucleating site for either the eutectic phase or the $Al_{11}Ce_3$ intermetallic. As the cooling rate decreases, the eutectic $Al_{11}Ce_3$ intermetallic particles, having longer formation times, lead to an increase in their particle size. The form of the intermetallic of $Al_{11}Ce_3$, both primary intermetallic and eutectic, was in concurrence with prior literature that has described in detail the shape of $Al_{11}Ce_3$ intermetallic as a function of Ce wt.%.[31] The intermetallic initially formed as rods, but as the weight percent of Ce increases, they start transforming into angular structures with two and three sides and finally creating an enclosed but hollow structure as shown in Figure 3.

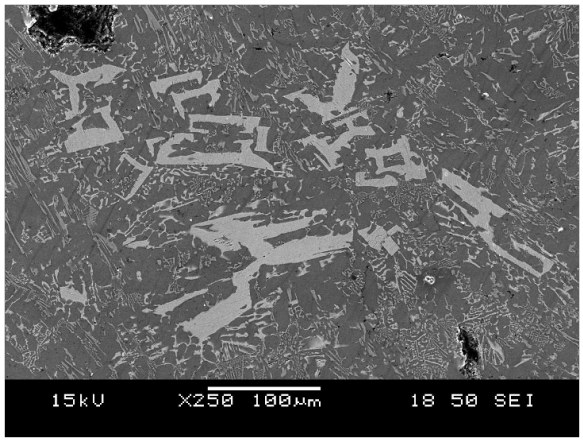

Figure 3. Cerium-rich intermetallic forms the distinct angular and enclosed structures as well as the eutectic phase in section B.

The slowest cooling rate had the lowest quantity of primary intermetallic, but the ones that formed were the angular structures and enclosed structures. As the cooling

rate decreased, the concentration of three-side angular and enclosed structures increased in the following sections. The enclosed structures contained a hollow interior region that formed a eutectic structure, as reported in prior studies with the base alloy.[32] The Al-Ce eutectic formed in the microstructure is comprised of two forms, the first being a lamellar structure, while another structure forms tightly packed boxes of angular lamellae. This observation has been discussed in prior literature.[18] An effect of the addition of reinforcement particles was the occasional disruption in the growth of intermetallic. If an Al-Ce intermetallic rod encountered a Ni-graphite particle during its growth, the reinforcement would block its propagation in that direction.

The image analysis of the microstructure shows that the area percentage of graphite particles remains fairly consistent throughout the different sections, with the fastest cooling rate at 7.46% and the slowest cooling rate at 5.88% by area. The porosity present in the casting was also observed to be a function of the cooling rate, with a slower cooling rate decreasing the formation of porosities in the casting as seen in Figure 4.

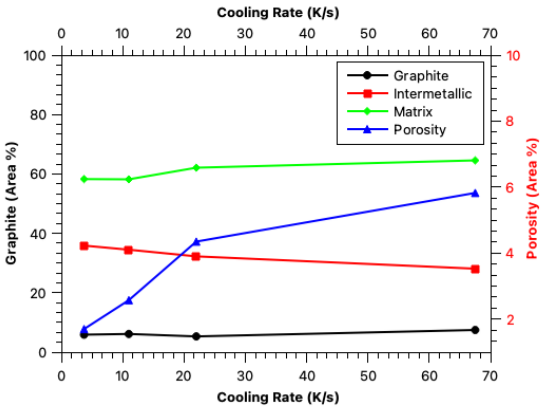

Figure 4. The distribution of the matrix, reinforcement, and intermetallic in the composite as a function of cooling rate and increase in area percent porosity with an increase in the cooling rate.

The absence of agglomerated particles suggests uniform mixing during the stirring process. The cooling rate of the melt showed a variation in the average primary intermetallic size and the average eutectic lamellar spacing. As the cooling rate decreases, the lamellar spacing increases. This similar trend was observed with the formation of primary intermetallic, where, as the cooling rate decreases, the time available for the growth of these particles increases. As observed in Figure 5, this leads to an increase in the size of the primary intermetallic of $Al_{11}Ce_3$.

The Al-Ce eutectic formed in the composite exhibited two structures, a lamellar structure and an enclosed structure comprised of angular lamellae, previously reported in the literature on Al-Ce binary alloys.[28]

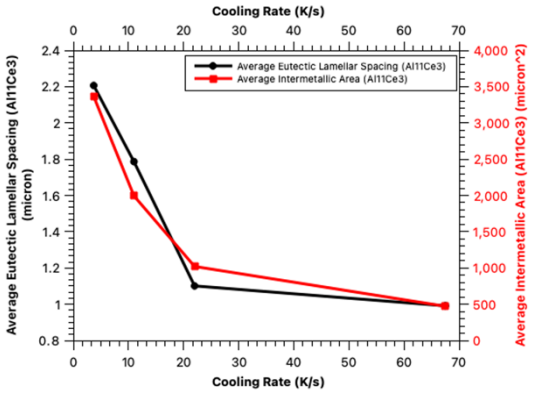

Figure 5. The variation of average primary intermetallic area and eutectic lamellar spacing as a function of cooling rate for the $Al_{11}Ce_3$.

In contrast, the Al-Ni intermetallic tended to form rectangular bars. At room temperature, both Ce and Ni have extremely limited solubility in Al.[33,34] The presence of Mg was detected in the α-Al phase. Mg has been used in Al alloys to improve their corrosion resistance as well as to improve the wettability of the melt with reinforcement particles. It should be taken into account that the addition of Mg in larger quantities, such as in the case of Al-8Ce-10Mg alloys, can lead to brittleness on account of higher hardness.[35]

Three primary phase peaks were identified using XRD, confirming the presence of $Al_{11}Ce_3$, Al_3Ni, and α-Al. The peak intensity of the Al_3Ni phase decreases as the cooling rate decreases, which was previously observed in Figure 6 (in the Appendix) using image analysis, while the peak intensity for $Al_{11}Ce_3$ increased.

The ternary phase diagram of the Al-Ce-Ni system provides insight into the phases formed during the solidification process. At a temperature of 1382F (750C), the Ni from the Ni-coated graphite will be dissolved in liquid Al, which also contains Ce. Based on the quantities provided in the materials and methods section, the composition of the liquid, under ideal conditions, is calculated to be 82 wt.% Al, 12 wt.% Ce, 2 wt.% Ni, and 2.5 wt.% Mg. In the ternary phase diagram of the set composition, the expected phases formed include $Al_{11}Ce_3$ and Al_3Ni. While the binary phase diagram of Ni-Ce shows reaction products forming, such as Ce_7Ni_3, this reaction product has not been reported in prior literature on the Al-Ce-Ni alloy system or observed in this study.[28,36]

The solidification pathway for the ternary system was determined based on the phase diagrams for the ternary system available at various temperatures. At 1472F

(800C), for the provided composition, the expected phases present in the system would be L + $Al_{11}Ce_3$, with $Al_{11}Ce_3$ formed as $\alpha Al_{11}Ce_3$.[37] Following the precipitation of $Al_{11}Ce_3$, on further cooling, the next phase to precipitate is Al_3Ni, as seen in Figure 7 (b) (in the Appendix). There are mentions of a ternary intermetallic forming between Al-Ce-Ni, but this was not observed in the samples, regardless of the cooling rate. The composition in this system lies under the curve wherein the formation of the τ_8 was observed, where τ_8 was a $Al_{23}Ce_4Ni_6$ intermetallic.[37–39]

The cooling curves shown in Figure 8 (in the Appendix) were obtained using the Solution Founderie Thermal Analysis equipment. The melt was held at 1562F (850C) while the Ni-graphite particles wrapped in a negligible amount of aluminum foil and preheated to 932F (500C) (58 wt.% Ni) were added up to 10 wt.% of the melt size using stir-mixing. The melt was poured into the solidification cup that was preheated to 1382F (750C), and the cooling curve was recorded. The various arrest points indicate the start of a phase formation, and the degree of undercooling and isotherm temperatures have been recorded in Table 3. Based on the composition of the alloy, the formation of $Al_{11}Ce_3$ precedes the formation of Al_3Ni. As the cooling rate of the melt decreases, the area percentage of the $Al_{11}Ce_3$ increases while Al_3Ni decreases. This is expected as a slower cooling rate will preferentially benefit the growth of the primary precipitating phase. It should be further noted that in an Al-Ce-Ni melt, at the melt stirring temperature, the melt is a suspension of L + $Al_{11}Ce_3$, thus, as the melt solidifies at a slower rate, the size of $Al_{11}Ce_3$ particles increases. The thermal arrest points were identified for the Al-Ce-Ni-Graphite cooling curve, indicating the formation of $Al_{11}Ce_3$, Al_3Ni, and the eutectic phase during solidification. The binary Al-12Ce alloy had the highest degree of undercooling, while the addition of alloying elements Ni and Mg led to a decrease in the undercooling. As Ni-graphite particles were incorporated in the melt, the undercooling reached its lowest point, as the graphite particles act as nucleation sites. The addition of graphite particles led to the shortest local solidification time.

Table 3. Undercooling and Freezing Isotherm Temperatures Measured Experimentally

System	DT	Isotherm Temperature
Al-12Ce	6.908°F (3.838°C)	1191.2F (644C)
Al-12Ce-4Ni	2.723°F (1.523°C)	1158F (626C)
Al-12Ce-2.5Mg	2.706°F (1.503°C)	1158F (626C)
Al-12Ce-4Ni-2.5Mg	2.117°F (1.176°C)	1119F (604C)
Al-12Ce-Ni-Graphite	<0.72°F (<0.4°C)	1157F (625C)

ELEMENTAL ANALYSIS AND PHASE FORMATION

The composition of the intermetallic was quantified using Point and ID analysis. Based on the phase diagrams discussed in the prior section, intermetallic rich in Ce and Ni were identified along with αAl. The Ce-rich eutectic showed a distinct lath formation, some of which formed the angular shape, while the Ni-rich intermetallic formed smaller box-shaped particles. In Figure 9 (in the Appendix), the section with the fastest cooling rate, a fine eutectic structure, was observed at high magnifications. The Ce-rich intermetallic further formed primary intermetallic, as seen in Figure 9 (b) (in the Appendix), and an area compositional analysis confirmed that the Ni (green) was present over the entire microstructure in the form of secondary intermetallic and eutectic and not concentrated around the graphite particles. The Ce (blue) distribution covers areas rich in intermetallic and eutectics as Ce does not have any solubility in Al. The presence of Mg in the microstructure was detected in the αAl as Mg has a solubility of up to 15 wt.% at its maximum.

Figure 9 (c) (in the Appendix) focuses on the Ce-rich eutectic phase in the microstructure, the isolated section highlighted in Figure 9 (b). The variation of Ce and Al concentration was clearly visible on the lamellar growth of the eutectic, with Ce decreasing as Al increased and vice versa. As the cooling rate decreased, the increase in the size of Ce-rich intermetallic is observed in Figure 10 (a), with an 'H' shaped particle precipitating. The intermetallic was surrounded by colonies of the eutectic phase and the αAl phase. On performing a compositional analysis of the intermetallic, it was confirmed that the particle was rich in Ce, forming the $Al_{11}Ce_3$ intermetallic. The matrix surrounding the particle shows the presence of Mg, which was on account of Mg addition during the casting process, as Mg has solubility in Al.

The section with the second fastest cooling rate, Figure 10 (in the Appendix), showed an increase in the size of the Ce-rich primary intermetallic. The primary intermetallic and eutectic structures were analyzed for their compositions. The composition of the eutectic phase observed in this study was in agreement with a prior study conducted on Al-Ce-Ni-Mn alloy.[40] As the cooling rate further decreased, the formation of Ce-rich primary intermetallic increased. Figure 11 (in the Appendix) shows the formation of these intermetallic at a smaller scale, observed in the inset picture. The elemental distribution of the microstructure shows Ce-rich areas, while the Ni was concentrated in areas around the eutectic. This was further confirmed with point analysis of the eutectic structure which quantified the Ni content.

HARDNESS AND DENSITY MEASUREMENTS

Figure 12 shows the hardness of the composite that was measured using the Rockwell F indentation method. As Ni dissolved into the melt during the stir-casting process and precipitated out during solidification in the form of

intermetallic, the hardness of the composite was higher than that of the base Al-12Ce alloy reported in the literature. Magnesium as a solid solution strengthener is present in the melt up to 2.5 wt.%. This would lead to an increase in the hardness of the matrix. In prior work on Al-Ce-Mg alloys, the effect of the addition of Mg on the hardness measured using Vickers Hardness showed that an increase in the Mg in solid solution led to a rise in the solid solution hardening of the αAl.[35] Additionally, the presence of graphite particles was expected to increase the hardness of the casting. In the section with the highest cooling rate, an increased grain refinement along with smaller intermetallic leads to increased hardness, which decreases with a slower cooling rate as the intermetallic gets larger.

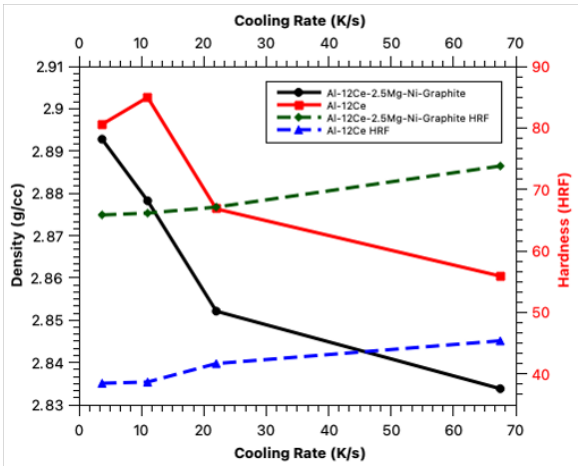

Figure 12. The variation of density (solid) and hardness (dash) on account of the variation in cooling rate.

The density of the composite was lower than the density of the base Al-12Ce alloy reported in the literature.[32] As the cooling rate decreased, there was an increase in the density of the composite as seen in Figure 13. This can be attributed to an increase in the proportion of the primary $Al_{11}Ce_3$ phase, which has a significantly higher theoretical density 4.17 g/cm^3 (0.15 lb/in^3) than the matrix.[41] The density of Al_3Ni has been reported as 4.03 g/cm^3 (0.145 lb/in^3), and the density of graphite is in the range of 2.09 – 2.26 g/cm^3 (0.075 – 0.081 lb/in^3).[42,43] The variation of the primary phases in different section sizes causes different densities in sample A-D. In other words, by increasing the section size, the cooling rate decreases (section D has a lower cooling rate). Additionally, alloying elements are rejected at the solidification front, leading to a higher concentration of alloying elements in sections with longer solidification times. Consequently, by increasing the thickness, larger primary and secondary phases with higher content are present, which leads to an increase in density as the section thickness increases.

CONCLUSIONS

The study of Al-Ce alloys has been crucial in the development of high-temperature stable and lightweight aluminum alloys. The addition of graphite particles as a reinforcement to form high-temperature stable composites would further industries such as the automotive industry in producing light-weight and efficient engines. The effect of cooling rate on the solidification, microstructural evolution, and select properties of the Al-12Ce-2.5Mg-Ni-Graphite composite was characterized in this work. The utilization of stirring during the casting process led to a uniform distribution of Ni-coated graphite particles across the matrix. As the cooling rate increased, the volume percentage of porosities formed in the matrix increased by 70.81%, which led to a 1.408% increase in the density of the composite. The size of the $Al_{11}Ce_3$ primary intermetallic and $Al_{11}Ce_3$ lamellar eutectic spacing was found to be a function of the cooling rate having an inverse correlation, wherein an increase in the cooling rate decreased both parameters by 85.98% and 55.071%, respectively. The hardness of the composite was inversely related to the cooling rate, with a 10.77% decrease in the HRF value. On comparison with the hardness of the Al-12Ce base alloy, there was an average increase of 39% in the HRF value.

REFERENCES

1. Latha Shankar, B., Anil, K. C., and Patil, R. “A Study on 3-Body Abrasive Wear Behaviour of Aluminium 8011 / Graphite Metal Matrix Composite,” *IOP Conference Series: Materials Science and Engineering*, V. 149, 012099 (2016).
2. Fu, H., Huang, Y., Wu, H., et al. “Synthesis by Vacuum Infiltration, Microstructure, and Thermo-Physical Properties of Graphite-Aluminum Composite,” *Advanced Engineering Materials*, V. 18, No. 9, 2016, pp. 1609–15.
3. Krishnamurthy, L., Sridhara, B. K., and Budan, D. A. “Comparative Study on the Machinability Aspects of Aluminium Silicon Carbide and Aluminium Graphite Composites,” *Materials and Manufacturing Processes*, V. 22, Nos. 7–8, 2007, pp. 903–8 (2007).
4. Mayer, H., and Papakyriacou, M. “Fatigue behaviour of graphite and interpenetrating graphite–aluminium composite up to 109 load cycles,” *Carbon*, V. 44, No. 9, 2006, pp. 1801–7.
5. Anil, K. C., Kumaraswamy, J., Reddy, M., et al. “Mechanical Behaviour and Fractured Surface Analysis of Bauxite Residue and Graphite Reinforced Aluminium Hybrid Composites,” *Frattura ed Integrità Strutturale*, V. 16, No. 62, 2022, pp. 168–79.
6. Ma, B., Wang, J., Lee, T. H., et al. “Microstructural characterization of Al4C3 in aluminum–graphite composite prepared by electron-beam melting,”

Journal of Materials Science, V. 53, No. 14, 2018, pp. 10173–80.
7. Chen, J. K., and Huang, I. S. “Thermal properties of aluminum–graphite composites by powder metallurgy,” *Composites Part B: Engineering*, V. 44, No. 1, 2013, pp. 698–703.
8. Sims, Z. C., Rios, O. R., Weiss, D., et al. “High performance aluminum–cerium alloys for high-temperature applications,” *Materials Horizons*, V. 4, No. 6, 2017, pp. 1070–8.
9. Zhang, A., and Li, Y. “Thermal Conductivity of Aluminum Alloys—A Review,” *Materials*, V. 16, No. 8, 2023, p. 2972.
10. Li, Y., Yu, Q., Chen, F., et al. “Effect of Sc on Al3Fe phase and mechanical properties of as-cast AA5052 aluminum alloy,” *China Foundry*, V. 21, No. 3, 2024, pp. 257–64.
11. Kharitonov, D. S., Örnek, C., Claesson, P. M., et al., “Corrosion Inhibition of Aluminum Alloy AA6063-T5 by Vanadates: Microstructure Characterization and Corrosion Analysis,” *Journal of The Electrochemical Society*, V. 165, No. 3, 2018, pp. C116–26.
12. Kaufman, J.G. “Fracture Resistance of Aluminum Alloys.” In: Anderson, K., Weritz, J., Kaufman, J. G., eds. "Properties and Selection of Aluminum Alloys," ASM International, 2019, pp. 33–51.
13. Tokisue, H., and Abbaschian, G. J. “Friction and wear properties of aluminum-particulate graphite composites,” *Materials Science and Engineering*, V. 34, No. 1, 1978, pp. 75–8.
14. Peng, X., Ying, H., Sun, X., et al. “High thermal conductivity and low thermal expansion coefficient of isotropic graphite-reinforced aluminum matrix composites prepared by in situ curing of silicon aerogel,” *Journal of Materials Science: Materials in Electronics*, V. 31, No. 12, 2020, pp. 9250–9.
15. Czerwinski, F. “Thermal Stability of Aluminum Alloys,” *Materials*, V. 13, No. 15, 2020, p. 3441.
16. Weiss, D. “Improved High-Temperature Aluminum Alloys Containing Cerium,” *Journal of Materials Engineering and Performance*, V. 28, No. 4, 2019, pp. 1903–8.
17. Sims, Z. C., Weiss, D., McCall, S. K., et al. “Cerium-Based, Intermetallic-Strengthened Aluminum Casting Alloy: High-Volume Co-product Development,” *JOM*, V. 68, No. 7, 2016, pp. 1940–7.
18. Czerwinski, F., and Shalchi Amirkhiz, B. “On the Al–Al11Ce3 Eutectic Transformation in Aluminum–Cerium Binary Alloys,” *Materials*, V. 13, No. 20, 2020, p. 4549.
19. Asthana, R. “Infiltration processing of silicon carbide platelet-reinforced aluminum alloy composites.” University of Wisconsin-Milwaukee, Milwaukee, 1991.
20. Asthana, R., Singh, M., and Sobczak, N. “The Role of Wetting and Reactivity in Infiltration of Ceramic-Metal Composites.” In: Zhu, D., Plucknett, K., eds. Ceramic Engineering and Science Proceedings, vol. 26. Hoboken, NJ, USA, John Wiley & Sons, Inc., 2005, pp. 248–61.
21. Rohatgi, P. K., Gupta, N., Schultz, B. F., et al. “The Synthesis, compressive properties, and applications of metal matrix Syntactic foams,” V. 63, No. 2, 2011.
22. Santa Maria, J. A., Schultz, B. F., Ferguson, J. B., et al. “Effect of hollow sphere size and size distribution on the quasi-static and high strain rate compressive properties of Al-A380–Al2O3 syntactic foams,” *Journal of Materials Science*, V. 49, No. 3, 2014, pp. 1267–78.
23. Bienia, J., Walczak, M., Surowska, B., et al. “Microstructure And Corrosion Behaviour Of Aluminum Fly Ash Composites,” n.d.
24. Rajan, T. P. D., Pillai, R. M., Pai, B. C., et al., “Fabrication and characterisation of Al–7Si–0.35Mg/fly ash metal matrix composites processed by different stir casting routes,” *Composites Science and Technology*, V. 67, Nos. 15–16, 2007, pp. 3369–77.
25. Rohatgi, P. K., and Weiss, D. “Casting of Aluminum - Fly Ash Composites for Automotive Applications,” *SAE 2003 World Congress & Exhibition*, 2003, 2003-01–0825.
26. Rohatgi, P. K., Gupta, N., and Alaraj, S. “Thermal Expansion of Aluminum–Fly Ash Cenosphere Composites Synthesized by Pressure Infiltration Technique,” *Journal of Composite Materials*, V. 40, No. 13, 2006, pp. 1163–74.
27. Rohatgi, P. K., Guo, R. Q., Iksan, H., et al., “Pressure infiltration technique for synthesis of aluminum–fly ash particulate composite,” *Materials Science and Engineering: A*, V. 244, No. 1, 1998, pp. 22–30.
28. Czerwinski, F. “Cerium in aluminum alloys,” *Journal of Materials Science*, V. 55, No. 1, 2020, pp. 24–72.
29. Okamoto, H. “Al-Ce (Aluminum-Cerium),” *Journal of Phase Equilibria and Diffusion*, V. 32, No. 4, 2011, pp. 392–3.
30. Cao, Z., Kong, G., Che, C., et al. “Experimental investigation of eutectic point in Al-rich Al-La, Al-Ce, Al-Pr and Al-Nd systems,” *Journal of Rare Earths*, V. 35, No. 10, 2017, pp. 1022–8.
31. Czerwinski, F., and Shalchi Amirkhiz, B. “On the Al–Al11Ce3 Eutectic Transformation in Aluminum–Cerium Binary Alloys,” *Materials*, V. 13, No. 20, 2020, p. 4549.
32. Behera, S. K., Van Hoogstraten, J., Rane, K. K., et al. “The Effect of Cooling Rate on the Microstructure and Physical Properties of Hypereutectic Al–Ce Alloys,” *International Journal of Metalcasting*, V. 18, No. 1, 2024, pp. 6–13.
33. Okamoto, H. “Al-Ni (Aluminum-Nickel),” *Journal of Phase Equilibria & Diffusion*, V. 25, No. 4, 2004, pp. 394–394.

34. Okamoto, H. “Al-Ce (Aluminum-Cerium),” *Journal of Phase Equilibria and Diffusion*, V. 32, No. 4, 2011, pp. 392–3.
35. Nam, S., Simsek, E., Argibay, N., et al. “Strength mechanisms and tunability in Al-Ce-Mg ternary alloys enabled by additive manufacturing,” *Materials & Design*, V. 231, 2023, p. 112009.
36. Belov, N. A., Naumova, E. A., and Eskin, D. G. “Casting alloys of the Al–Ce–Ni system: microstructural approach to alloy design,” *Materials Science and Engineering: A*, V. 271, Nos. 1–2, 1999, pp. 134–42.
37. Raghavan, V. “Al-Ce-Ni (Aluminum-Cerium-Nickel),” *Journal of Phase Equilibria and Diffusion*, V. 30, No. 3, 2009, pp. 265–7.
38. Wang, H., Li, Z., Chen, Z., et al. “Thermodynamic Optimization of the Ni-Al-Ce Ternary System,” *Journal of Phase Equilibria and Diffusion*, V. 37, No. 2, 2016, pp. 222–8.
39. Tang, C., Du, Y., Xu, H. H., et al. “Experimental investigation of the Al–Ce–Ni system at 800°C,” *Intermetallics*, V. 16, No. 3, 2008, pp. 432–9.
40. Kozakevich, J. R., Stroh, J., Sediako, D., et al. “Solidification Kinetics of an Al-Ce Alloy with Additions of Ni and Mn,” *Metals*, V. 13, No. 5, 2023, p. 955.
41. Wu, T., and Dunand, D. C. “Microstructure and thermomechanical properties of Al11Ce3,” *Intermetallics*, V. 148, 2022, p. 107636.
42. The Materials Project, “Materials Data on Al3Ni,” 2020-07-14. https://doi.org/10.17188/1278109
43. Robinson, G. R., Jr., Hammarstrom, J. M., and Olson, D. W. “Critical mineral resources of the United States—Economic and environmental geology and prospects for future supply: U.S. Geological Survey Professional Paper 1802,” 2017.
44. Zhang, H. X., Dai, J. J., Sun, C. X., et al. “Wear Rate and Thermal Conductivity of a Copper-Plated Graphite Flake/Aluminum Composite,” *Journal of Electronic Materials*, V. 48, No. 11, 2019, pp. 7585–92.
45. Huang, Y., Su, Y., Guo, X., et al., “Fabrication and thermal conductivity of copper coated graphite film/aluminum composites for effective thermal management,” *Journal of Alloys and Compounds*, V. 711, 2017, pp. 22–30.
46. Lin, C. B., Wang, T. C., Chang, Z. C., et al., “Tribological Analysis of Copper-Coated Graphite Particle-Reinforced A359 Al/5 wt.% SiC Composites,” *Journal of Materials Engineering and Performance*, V. 22, No. 1, 2013, pp. 94–103.
47. Jiang, D., Zhu, X., and Yu, J. “Enhanced Thermal Conductivity and Bending Strength of Graphite Flakes/aluminum Composites Via Graphite Surface Modification,” *Journal of Wuhan University of Technology-Mater. Sci. Ed.*, V. 35, No. 1, 2020, pp. 9–15.
48. Chu, H. Y., and Lin, J. F. “Experimental analysis of the tribological behavior of electroless nickel-coated graphite particles in aluminum matrix composites under reciprocating motion,” *Wear*, V. 239, No. 1, 2000, pp. 126–42.
49. Ted Guo, M. L., and Tsao, Chi.-Y. A. “Tribological behavior of aluminum/SiC/nickel-coated graphite hybrid composites,” *Materials Science and Engineering: A*, V. 333, Nos. 1–2, 2002, pp. 134–45.
50. Han, X., Huang, Y., Gao, Q., et al., “High Thermal Conductivity and Mechanical Properties of Nanotube@Cu/Ag@Graphite/Aluminum Composites,” *Industrial & Engineering Chemistry Research*, V. 57, No. 31, 2018, pp. 10365–71.
51. Fuentes, R., Rubio, E., Gómez, C., et al. “Wear behavior of a self-lubricating aluminum/graphite composite prepared by powder metallurgy,” *Industrial Lubrication and Tribology*, V. 55, No. 4, 2003, pp. 157–61.

APPENDIX

OVERSIZE FIGURES AND TABLES
(ON THE FOLLOWING PAGES)

APPENDIX—OVERSIZE FIGURES AND TABLES

Table 1. Comprehensive Review of the Matrix, Reinforcement, Fabrication Method, and Select Properties of Aluminum-Based Metal Matrix Composites.

Matrix	Reinforcement	Casting Method	Volume Fraction	Wear	COF	Bending Strength	Thermal Conductivity	CTE	Ref #
Pure Al	Cu-coated Graphite	Hot Press Sintering	40-70%	$2.31x10^{-7}mm^3/Nmm$	0.171		328-612 W/mK		44
1060 Al Foil	Cu-coated Graphite	Vacuum Hot Processing	17.4-53.2%				397-805 W/mK		45
A359	SiC and Cu-coated Graphite	Squeeze Casting		Decline	Decline				46
A356	Ni and Cu coated Graphite	Pressure Infiltration	30-70%			20.4-59.3 MPa	335-515 W/mK		47
Al7Si1Mg	Ni-coated Graphite	Stir Casting		Decline	Decline				13
Al6061	SiC and Natural Graphite	Hot Compaction and Extrusion		$51.3x10^{-9}$ – $1.19x10^{-9}$ g/m	0.26-0.018 (Wet) 0.63-0.55 (Dry)				48
Al6061	SiC and Ni-coated Graphite	Semi-solid powder densification			0.72			$13x10^{-6}/K$	49
Pure Al	Natural Flake Graphite	Hot Pressing	10-90%				324-783 W/mK	16.9 to -2.5 ppm/K (Parallel to Basal) 15.2 to 10.1 ppm/K (Perpendicular to Basal)	7
Aluminum 8011	50-micron graphite powder	Two step stir casting	8 wt.%	(30min 10kg): rate 0.789; (30min 20kg): rate 1.5947; (30min 30kg) rate: 1.9372					1
Pure Al	Uncoated Graphite	Vacuum gas pressure Infiltration	51%				105 W/mk	Lowest	14
Pure Al	Graphite coated in 4mass%Cu	Vacuum gas pressure Infiltration	54%				186 W/mk	Middle	14
Pure Al	Graphite coated in 8mass% Cu	Vacuum gas pressure Infiltration	53%				208 W/mk	Highest	14
Pure Al	No graphite, nanotube	Vacuum gas pressure Infiltration	0mm, 1wt.%			32.88 Mpa	266.16 W/mk		50
Pure Al	graphite, nanotube	Vacuum gas pressure Infiltration	0.1mm film, 1wt.%			34.89 Mpa	451.07 W/mk		50
Pure Al	graphite, nanotube	Vacuum gas pressure Infiltration	0.3mm film, 1wt.%			50.42 Mpa	324.87 W/mk		50

Pure Al	graphite, nanotube	Vacuum gas pressure Infiltration	1mm film, 1wt.%			76.05 Mpa	209.46 W/mk		[50]
Al+8wt.%RMp	Graphite particles	Stir Casting	2-10wt.%						[5]
Pure Al	No Graphite	Electron beam vacuum melting					226.7 W/mk		[6]
Pure Al	Graphite	Electron beam vacuum melting	4wt.%				107.8 W/mk		[6]
Pure Al	Graphite	Vacuum hot pressing	10%				16.9ppm/K Parallel Basal, 15.2ppm/K Perpendicular Basal		[7]
Pure Al	Graphite	Vacuum hot pressing	90%				-2.5ppm/K Parallel Basal, 10.1ppm/K Perpendicular Basal		[7]
Pure Al	Graphite	Sintering	3wt.%	Optimal, compared to pure Al and Al with 5 and 7wt.% graphite in both surface treated and untreated composites					[51]

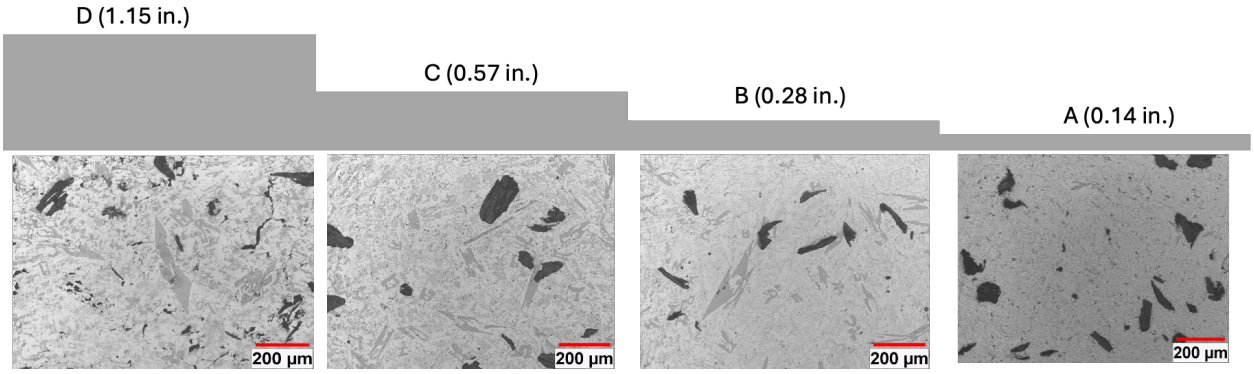

Figure 2. Unetched microstructure of the Al-12Ce-Ni-Graphite composite in different section sizes showing the uniformity in volume fraction of graphite particles in all sections. The section size increases from A to D.

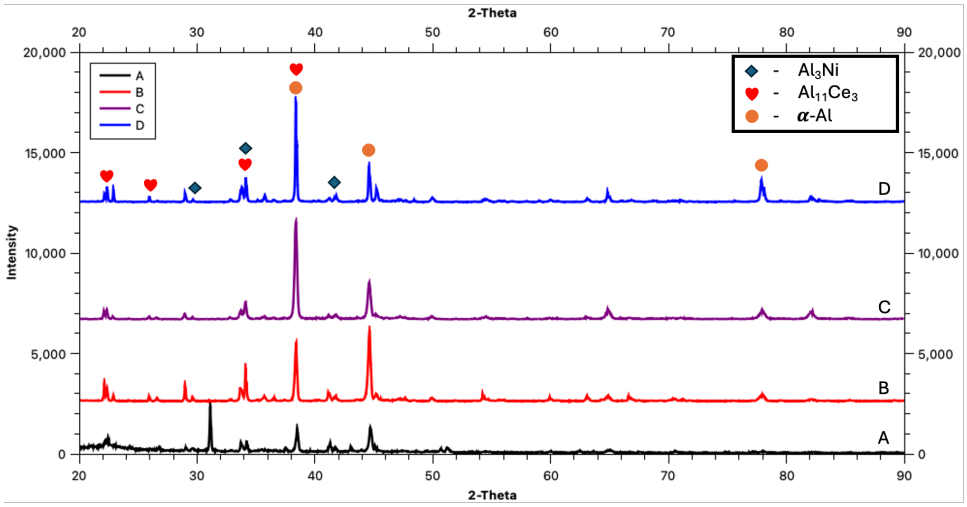

Figure 6. The XRD plot of the composite shows the identified phases.

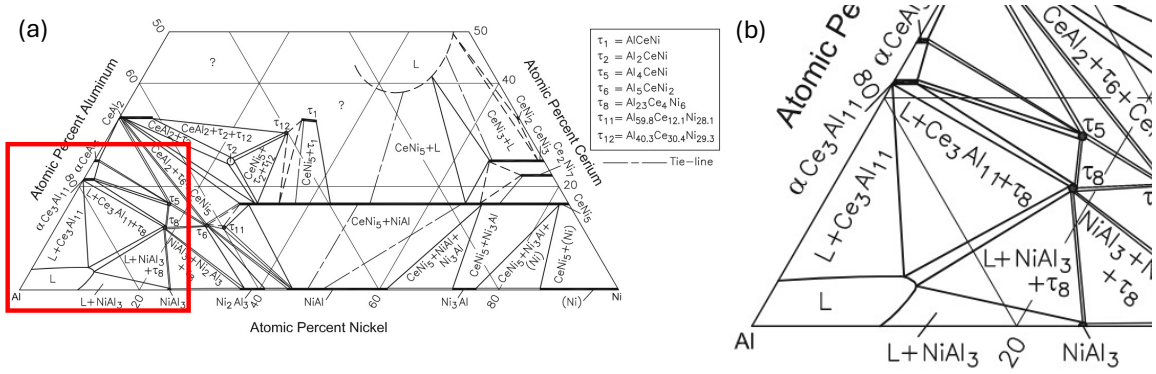

Figure 7. Al-Ce-Ni ternary phase diagram at the (a) 1472F (800C), (b) Magnified view of the nominal composition section.[37] (Artwork reprinted with permission.)

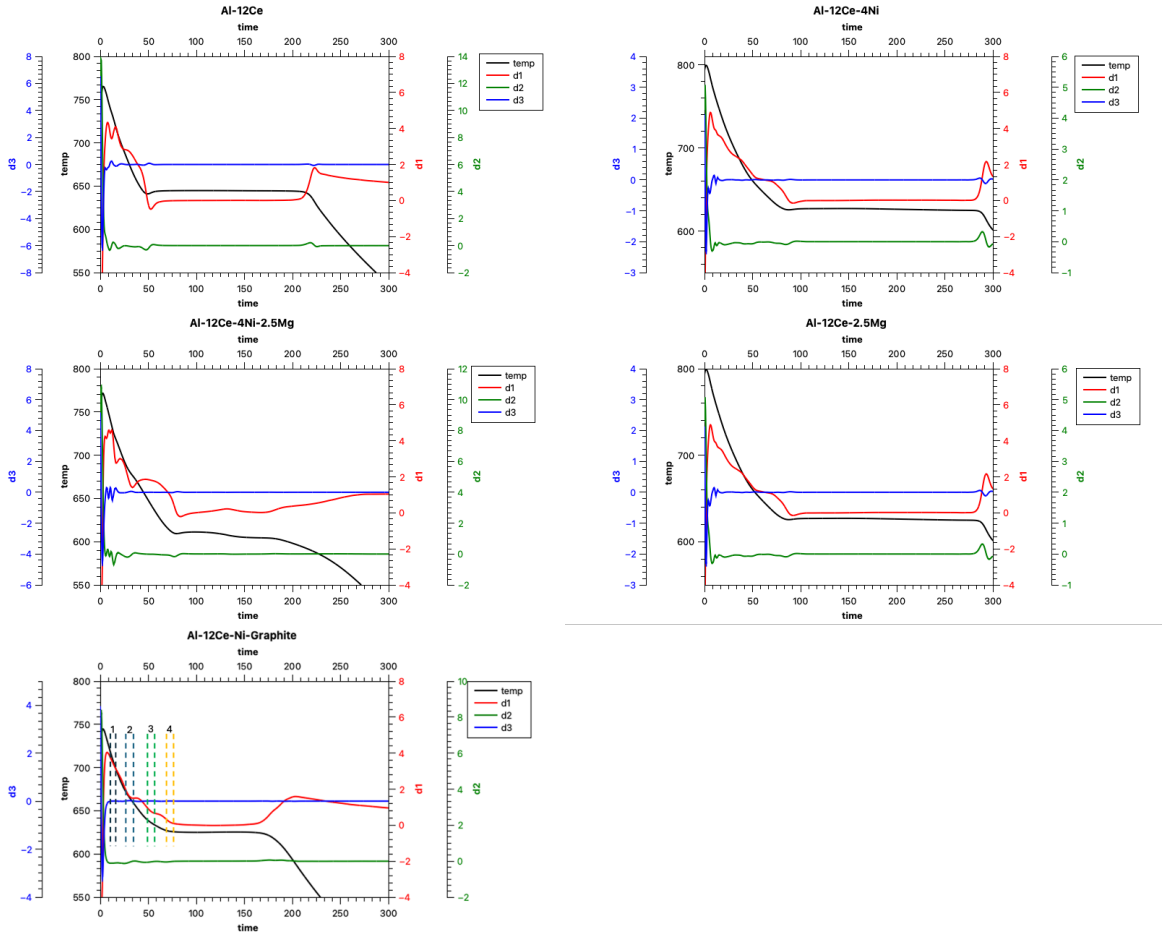

Figure 8. Cooling curve of the Al-12Ce base alloy, Al-12Ce-4Ni, Al-12Ce-4Ni-2.5Mg, Al-12Ce-Ni-Graphite, and Al-12Ce-2.5Mg showing the arrest points during solidification.

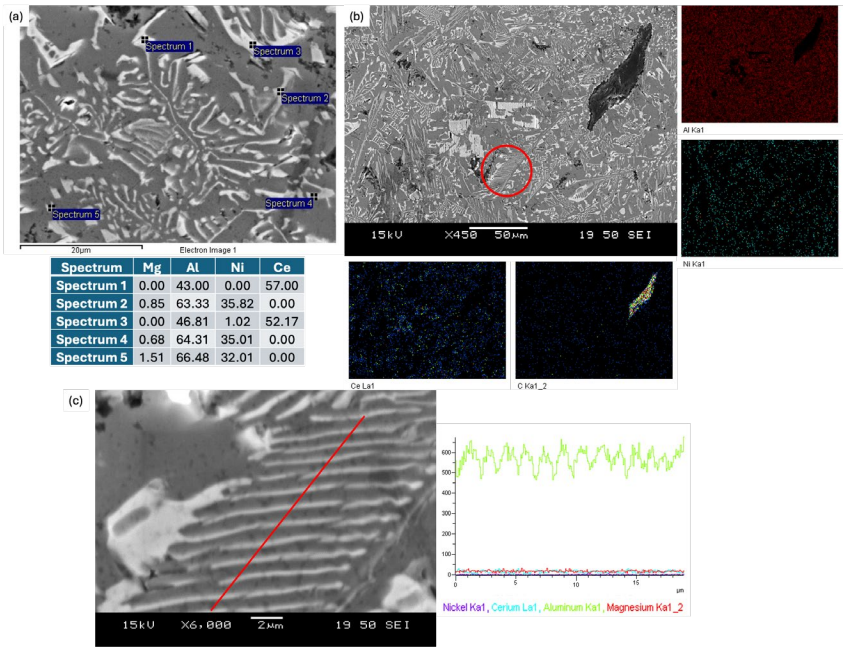

Spectrum	Mg	Al	Ni	Ce
Spectrum 1	0.00	43.00	0.00	57.00
Spectrum 2	0.85	63.33	35.82	0.00
Spectrum 3	0.00	46.81	1.02	52.17
Spectrum 4	0.68	64.31	35.01	0.00
Spectrum 5	1.51	66.48	32.01	0.00

Figure 9. (a) Point and ID of the intermetallic, (b) Compositional scans of Al, Ni, Ce, and C showing elemental distribution. (c) Compositional profile of the $Al_{11}Ce_3$ eutectic phase (highlighted in (b)) showing the variation of Al and Ce concentrations.

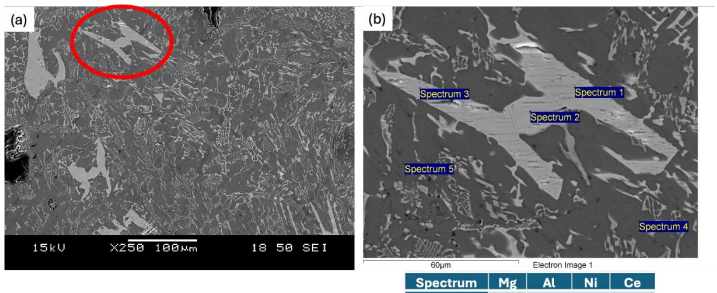

Spectrum	Mg	Al	Ni	Ce
Spectrum 1		40.53	0.00	59.47
Spectrum 2		40.40	0.00	59.60
Spectrum 3		40.68	0.00	59.32
Spectrum 4	3.53	96.47		
Spectrum 5	3.54	96.46		

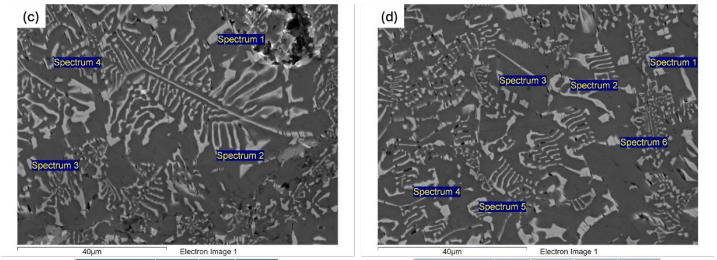

Spectrum	Al	Ni	Ce
Spectrum 1	42.19	0.00	57.81
Spectrum 2	53.12	1.20	45.68
Spectrum 3	46.32	1.32	52.36
Spectrum 4	53.02	0.00	46.98

Spectrum	Mg	Al	Ni	Ce
Spectrum 1		43.74	0.00	56.26
Spectrum 2		44.63	1.18	54.20
Spectrum 3		47.86	0.00	52.14
Spectrum 4		56.32	0.00	43.68
Spectrum 5		48.90	1.25	49.84
Spectrum 6	1.27	65.98	32.74	

Figure 10. (a) Section B from step mold showing larger Ce-rich intermetallic, (b) Compositional analysis of highlighted Ce-rich intermetallic and surrounding matrix, (c and d) The eutectic structure and chemical composition of the eutectic lamellae.

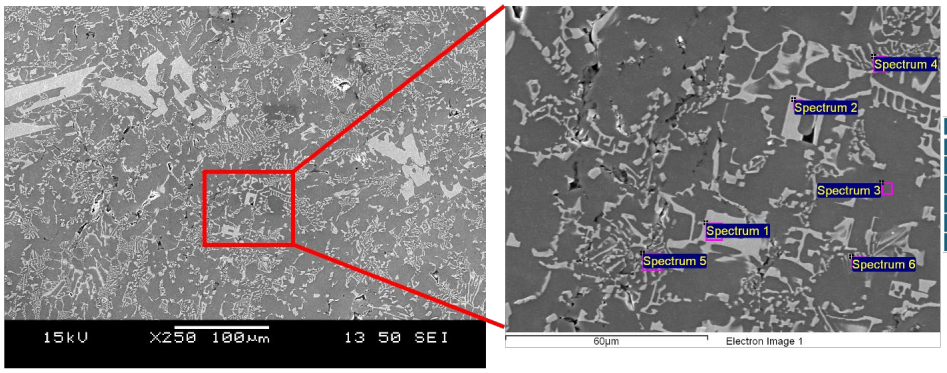

Spectrum	Mg	Al	Ni	Ce
Spectrum 1	0.00	40.16	0.00	59.84
Spectrum 2	0.00	39.72	0.00	60.28
Spectrum 3	2.90	97.10	0.00	0.00
Spectrum 4	1.65	83.00	15.35	0.00
Spectrum 5	2.78	78.39	9.21	9.62
Spectrum 6	1.29	81.01	17.70	0.00

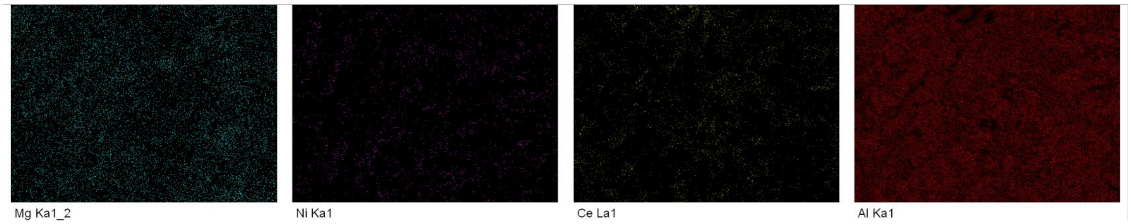

Figure 11. Compositional analysis of sample from section C of the step mold showing presence of hyper-eutectic Ce-rich intermetallic. The elemental scan shows the distribution of alloying elements in the inset picture confirming the presence of Ce-rich and Al-rich areas.